The effect of contact pressure on photoplethysmography

Xin Gong, Chengbo Yu, Yiguo Xuan

College of Electrical and Electronic Engineering, Chongqing University of Technology, Chongqing, China

Article Info	ABSTRACT
	In the bioinformation photoplethysmography (PPG) measurement, the precision and repeatability could be impacted by the contact pressure between the optical sensor and the measurement site. Taking the finger's geometrical, mechanical, and optical characteristics into consideration, finite element models and Monte Carlo (MC) simulation methods were used to quantitatively analyze the effects of the deformation of different finger layers under contact pressure on its optical parameters and PPG signals during fingertip spectroscopic detection. Firstly, a 3D axisymmetric finger model was established, pelican optimization was used to find the parameter lamp that caused the simulation to best match the finger pressing behavior, modeled the deformation of each layer, and quantified the changes in their absorption and scattering coefficient. Then, before and after pressure application, photon propagation in the reflectance and transmittance modalities within the diastolic and systolic finger tissues at 660 nm and 940 nm were studied by MC simulation. The result shows that contact pressure significantly altered the thickness of the dermis and subcutaneous tissues, a decrease in tissue thickness caused an increase in optical coefficient, which resulted in a reduction in normalized pulsatile reflectance and a boost in transmittance, and the change was dependent on wavelength.

Corresponding Author:

Chengbo Yu
College of Electrical and Electronic Engineering, Chongqing University of Technology
400054 Banan, Chongqing, China
Email: yuchengbo@cqut.edu.cn

1. INTRODUCTION

Photoplethysmography (PPG) is an optical technique for measuring volumetric changes in the pulsatile blood vessels [1]. Recording the intensity of reflected and transmitted light through the measured location, pulse wave signals could be obtained, which consists of arterial pulses period of each heartbeat, and plenty of biometric information can be detected [2]. The most typical application of PPG monitoring is transmission-mode finger pulse oximetry [3], whereas reflected PPG acquisition positions are more adaptable for wearable devices [4]. In recent years, research interest in PPG applications has grown beyond oximetry to encompass diabetes, hypertension, atherosclerosis, coronary artery disease, coronary heart disease, heart rate, and blood pressure monitoring [5].

During the vivo measurement, the morphology of the PPG would be influenced by many factors [6], [7]. The contact pressure between the optical sensor and the measurement site, in particular, causes changes in the optical and material properties of the skin, which impacts the detected spectral intensity and the effective information [8], [9]. Kamshilin *et al.* [10] analyzed the hand circulation during fingertip-sensor contact using a camera, from which an increase in the amplitude of the PPG signal was observed. May *et al.* [11] analyzed the effect of contact pressure on the 17 PPG morphological features by modeling artificial blood vessels, and pointed out that the influence of pressure must be included in the morphological study of

parameters such as oxygen saturation. Lim *et al.* [12] studied the variation of diffuse reflectance spectra with the pressure of the fiber-optic probe, and the results showed that the longer the pressure applied, the greater the spectral difference. Controlling the magnitude and duration of contact pressure can improve the quality of PPG signals. Reif *et al.* [13] reported that contact pressure affects the absorption and scattering coefficients of tissues to a certain extent. Li *et al.* [9] used a finite element model (FEM) of the dermis to simulate its deformation under pressure and built a Monte Carlo (MC) model to simulate the change of its absorption and scattering coefficients in the deformed tissue. He found that the pressure affects both the optical and material properties of the skin. Moco *et al.* [14] proved the importance of the role of blood in the fat layer in the formation of fingertip PPG by modeling a six-layer skin MC, which included the subcutaneous fat layer. Andreia declared that his model was simplified and that the effects of the skin site and layer properties (e.g., thickness and absorption-scattering properties) during the modeling process require further study. Simultaneously, all the models focus only on the effect of the cutaneous vasculature on the reflected PPG, and the effect of the optical interactions of all the absorbers present in all the pulsatile and non-pulsatile portions (including skin, fat, muscle, and bone) on the PPG during tissue deformation under pressure has never been investigated. Kwon *et al.* [15] constructed a functional model of the interaction between the thickness variation and the changes in absorption and scattering coefficients of each skin layer under external pressure. This model facilitates the analysis of light propagation in deformed tissues, to provide a quantitative and detailed analysis of the mechanism of influence between the light source's wavelength, the tissue deformation, the tissue optical parameters changes, and the spectrum.

In this study, the geometric, optical, and mechanical parameters of the left index finger were considered to analyze the impact of skin deformation on fingertip PPG collection, building on these models. Initially, the finger's pressing force over time and contact image that are processed to ascertain contact area are collected during the human subjects pressing on glass. The dynamic contact process is simulated and replicated in a finite finger model by parameter optimization search to find the best lumped parameter values that closely reproduce the finger press behavior, and the deformation of the multilayered tissue is decided, allowing the model to more accurately simulate the deformation of the finger during contact. The MC method is used to simulate the propagation of light in the finger and the changes in the transmitted and reflected PPG during pressure application, based on the research results of the relationship between thickness changes and its optical coefficients, and the effect of the contact pressure on the accuracy of the oximetry is further analyzed.

2. METHOD

2.1. Data collection and processing

This research utilized the apparatus depicted in Figure 1 to measure and record the variations in finger pressing force and contact area over time. The measurement device consists of a thin film pressure sensor (FlexiForce A201, Tekscan), signal amplification module (LM358, Onsemi), and processor (Arduino UNO, Arrow) at a sampling rate of 9,600 Hz and a resolution of 0.01 N, to record contact pressure. The fingerprint images are captured by a charge coupled device (CCD) industrial camera (SY8031, China), which has a resolution of 3,264×2,448 pixels, installed below the glass.

Experimental data was collected from the left index finger of a male subject. The finger was asked to be spotless, then pressed vertically on the center of the image acquisition field until the normal contact force reached 2 N, and repeated the data acquisition 15 times. It is worth noting that we do not limit the pressing speed or time. Due to the irreversibility of the simulation model, some points in the collected pressure data were removed in order to maintain a monotonic increase as the input to the FEM model. Calculating the accurate contact area from the original contact image requires several processing steps, including region of interest (ROI) extraction, image transformation, followed by background noise removal and threshold enhancement, and finally extracting the area corresponding to each pixel of the image (0.009325 mm2/pixel) multiplied by the pixels of the contact area to derive the total contact area. The processing steps are shown in Figure 2. The collected data after processing is shown in Figure 3. Figures 3(a) and Figure 3(b) show 15 groups of contact pressure and area derived after processing, respectively.

2.2. Finite element finger model

A 3D FEM of a male's left index finger was established by COMSOL Multiphysics, to model the development of the contact region between the finger and the optical sensor. The model was composed of five layers: fingernail, epidermis, dermis, subcutaneous tissue, and phalanx. Figure 4 describes the axially symmetric 3D finger model. The dimension parameters come from the literature [16]–[20]. This model proves a lower computational load than the non-axisymmetric model, enabling the repetition of the simulations with varying parameter combinations [16]. The optical sensor is abstracted as a glass plate with a

thickness of 10 mm. The material property parameters related to model development are listed in Table 1. Data are from the literature [17], [18], [21].
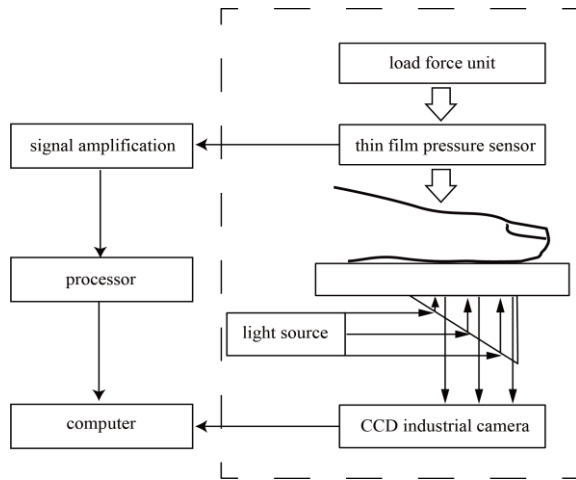

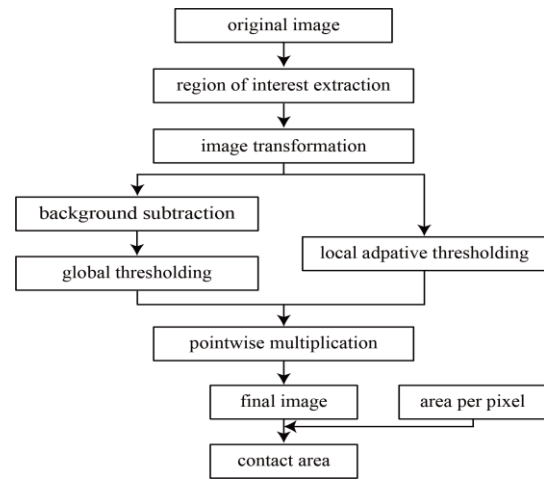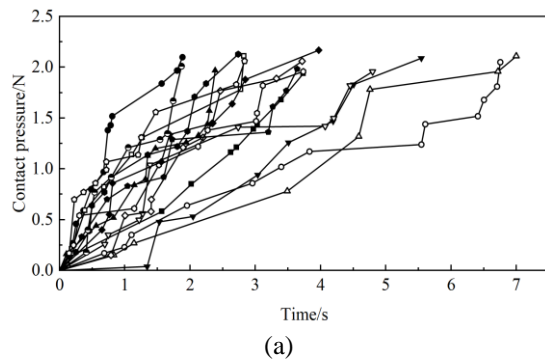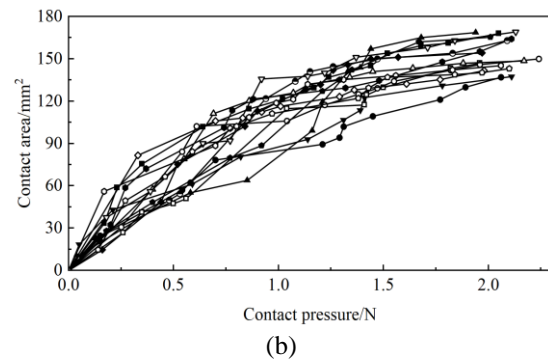Figure 1. Overall design for data acquisition system

Figure 2. Procedure for calculating the contact area

(a)

(b)

Figure 3. 15 sets of measurement data of (a) contact pressure over time and (b) variation of contact area with contact pressure
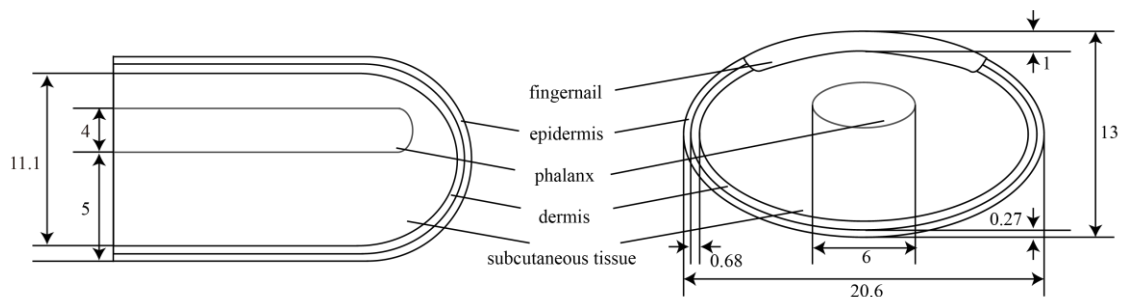

Figure 4. Longitudinal (left) and cross (right) sections of the axisymmetric 3D finger model and their geometric parameters (unit:mm)

Table 1. Material parameters of the finger finite element model

Parameter	Finger	Fingernail	Phalanx	Glass plate
Poisson's ratio (-)	0.48	0.3	0.3	0.2
Density (kg/m^3)	100	1900	1960	2700
Young's modulus (kPa)	10	1.7×10^5	1.7×10^6	9×10^7

The material properties of soft tissues (involving dermis and subcutaneous tissue) under small load are nonlinear and viscoelastic, a generalized Maxwell model with better capacity to capture the viscoelastic of human skin was chosen to characterize [22]. Fingernails, phalanx, and epidermis are linearly elastic [23]. The epidermis was modeled as linear and assigned it the parameter E_0. The material parameters of fingernail and phalanx were set by the fixed values in Table 1. Figure 5 shows the constitutive model of three-layer skin. E_0 is represented by a linear spring in this simulation. E_{v1} and τ_{v1}, E_{v2} and τ_{v2} both designated as Maxwell models. At a low strain rate, the skin can be expressed as:

$$\sigma = \sigma_e + \sigma_v \tag{1}$$

where σ_e stands for the stress part of the linear spring E_0, σ_v represents the stress part of the viscoelastic, i.e., the Maxwell part. The stress can be derived from the following ordinary differential equation from the stress equilibrium equation.

$$\sigma_e = \eta \frac{d\varepsilon_e}{dt} \tag{2}$$

$$\tau_{vm}\sigma_{vm} + \frac{d\sigma_{vm}}{dt} = \sigma_e \tag{3}$$

External strain is defined by the stress equilibrium equation of an ordinary differential equation as (4).

$$\varepsilon = \sum_{m=1}^{2} 2G_{vm}(\sigma_e + \sigma_{vm}) \tag{4}$$

Among the variables, ε denotes the total strain of the model, while G_{v1} and G_{v2} correspond to the shear modulus of the dermis and subcutaneous tissue, respectively. τ_{v1} and τ_{v2} represent the relaxation time of these two parts. $E = 2G(1+p)$ and $\tau = \eta/G$ are used to calculate the model parameters, where p is Poisson's ratio. The model input was derived from the contact pressure recorded in 15 experiments. Defined a contact pair between the skin model and the glass, utilizing the integration feature of COMSOL, the simulated contact area at each time can be obtained.
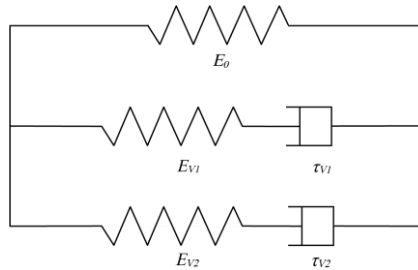

Figure 5. Skin constitutive model

2.3. Parameter optimization search

The actual contact area is $A_{(n,t)}$ at time t and force F_t. And the simulated contact area is a function of the lumped parameter $(E_0, E_{v1}, E_{v2}, \tau_{v1}, \tau_{v2})$, that is, $S_{(n,t)} = f_n(E_0, E_{v1}, E_{v2}, \tau_{v1}, \tau_{v2}, t, F_t)$. The objective function is defined as (5).

$$MSE = \frac{1}{15}\sum_{n=1}^{15}\left(A_{(n,t)} - S_{(n,t)}\right)^2 \tag{5}$$

We search for the optimal parameter values, with the objective of finding the parameter lump that enables the lowest sum of MSE across the 15 measurement experiments, to cause the model's simulated contact area to evolve in the same way as the contact area measured. Possible values were chosen by referring to the research on Young's modulus of each layer [22], which was reported as: 136 kPa for the epidermis, 80 kPa for the dermis, and 34 kPa for the subcutaneous tissue, and the simulation results of Nam and Kuchenbecker [16]. Then an artificial search for the values to maximize the objection function was conducted. Finally, the range was set as: $E_0(130000, 1550000)$, $E_{v1}(130000, 156000)$, $E_{v2}(22000, 60000)$, τ_{v1} and τ_{v2} both in $(0.4, 0.81)$. The model was executed to simulate the contact area for all parameter combinations.

A subset comprising 5% of the simulated contact area data was randomly chosen to create a new data set. The parameter combination that reached the lowest MSE in this data set was determined using the pelican optimization algorithm (POA), particle swarm optimization (PSO), and grey wolf optimizer (GWO), to ascertain the most suitable method for conducting parameter search across the entire dataset. The results of the comparison experiments are shown in Table 2. It becomes evident that the POA algorithm exhibits superior performance in the experimental dataset. Prior research has also shown that this algorithm shows greater competitiveness and superiority in solving optimization problems. To optimize parameters, the POA algorithm was chosen.

Table 2. Comparison of results of POA/PSO/GWO (unit: mm^4)

POA	PSO	GWO
7,731	9,248	9,434
8,036	9,772	9,459
8,350	9,218	9,557

2.4. Optical properties of skin

The anatomical feature of the finger is depicted in Figure 6. As can be seen in Figure 6(a), there are seven layers total: (A) skin, (B&F) fat, (C&E) muscle, and (D) phalanx. It should be noted that the cylindrical phalanx is located throughout the 10 mm-thick muscle layer. The model divides the skin layer into six stacked horizontal layers based on the inhomogeneity of the vascular distribution. The first and second layers are the stratum corneum and epidermis, with no blood. Melanin is distributed in these two layers and shows strong absorption in the visible range (400-760 nm) [24], [25]. The dermis is subdivided into four layers: (3) papillary dermis, (4) upper blood net dermis, (5) reticular dermis, and (6) deep blood net dermis, each containing a different volume of blood. Capillaries are distributed in the papillary dermis. The blood in the upper blood net dermis, reticular dermis, and deep blood net dermis represents the small arteries that supply the entire skin and the small veins that collect the recurring venous blood [26], followed by (7) fat, consisting of thicker and more dense collagen, elastin and adipocyte, which distributes the arteries and arterioles [27]. The overall structure is shown in Figure 6(b).
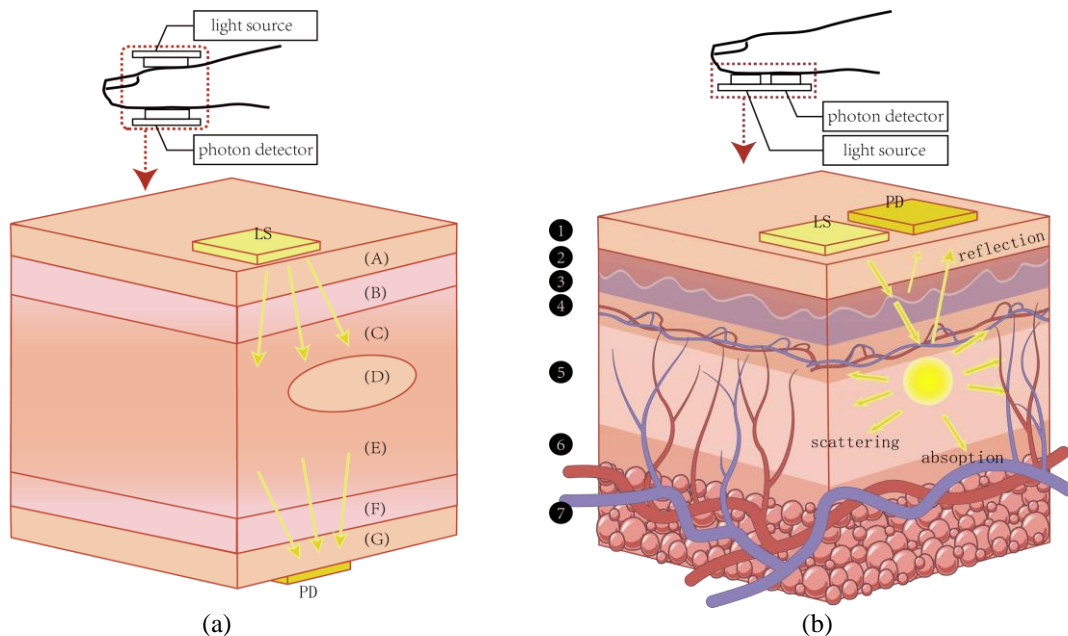

Figure 6. Photon transport in (a) reflective and (b) transmissive light source-detector mode

The thickness (d), diastolic blood volume (V_b), and water content (V_w) of each skin layers and the fat are shown in Table 3, with data derived from Chatterjee and Kyriacou [28]. A melanin content of 13% is considered in the model [29], as the volume of melanin in white people is set between 1.3% and 6.3%, yellow people between 11% and 16%, and black people between 18% and 43%.

Table 3. The parameters of thickness, blood volume, and water volume

Layer name	d (mm)	V_b	V_w
Stratum corneum	0.02	0	0.05
Epidermis	0.25	0	0.2
Papillary dermis	0.1	0.04	0.5
Upper blood net dermis	0.08	0.3	0.6
Reticular dermis	0.2	0.04	0.7
Deep blood net dermis	0.3	0.1	0.7
Fat	0.55	0.3	0.05

Figure 6 depicts the movement of photons after entering the fingertip. The optical properties of the tissue determine the depth and direction of photon transmission, primarily including absorption and scattering coefficients, and anisotropy factor [30]. The parameters related to absorption and scattering are shown in Figure 7. For each layer, scattering ($\mu_s(\lambda)$) and anisotropy ($g(\lambda)$) are wavelength dependent [24], [25]. The scattering properties are described as the sum of Mie scattering and Rayleigh scattering, which reflects the forward and backward scattering properties of each layer's cells, respectively. The scattering fraction due to Rayleigh scattering (f_{ray}) and the power of Mie scattering (b_{mie}) at 500 nm are shown in Figure 7(a).

$$\mu_s(\lambda) = a' \left[f_{ray} \left(\frac{\lambda}{500} \right)^{-4} + (1 - f_{ray}) \left(\frac{\lambda}{500} \right)^{-b_{mie}} \right] \tag{6}$$

$$g(\lambda) = 0.62 + 2.9\lambda \times 10^{-3} \tag{7}$$

Skin absorption is caused by its chromophores, predominantly melanin, water, oxyhemoglobin (HbO$_2$), and deoxyhemoglobin (HHb) [28], [29]. Figure 7(b) depicts the absorption factors of these four chromophores at 300-1,000 nm. Depending on the composition of the layers and their content, this paper has defined the absorption coefficient of each layer. The absorption coefficient of the stratum corneum and epidermis without blood is defined as (8).

$$\mu_a(\lambda) = V_m \mu_m(\lambda) + V_w \mu_w(\lambda) + (1 - V_m - V_w) \mu_b(\lambda) \tag{8}$$

In each layer of the dermis, the absorption of photons by arterial and venous blood with different concentrations of HbO$_2$ and HHb must be accounted, with the ratio of arterial to venous blood in the dermis set to 1:1 [31], and the oxygen saturation of arterial blood (SaO_2) and venous blood (SvO_2) set to be 70% [26]. The total absorption coefficient is expressed as (9).

$$\mu_{a_i}(\lambda) = V_{A_i} \mu_{A_i}(\lambda) + V_{V_i} \mu_{V_i}(\lambda) + V_{w_i} \mu_{W_i}(\lambda) + (1 - V_{A_i} - V_{V_i} - V_{w_i}) \mu_b(\lambda) \tag{9}$$

The chromophores in the fat layer are water, adipose tissue, and blood. The adipose concentration (V_{adi}) in the organization is set to 40% [14]. The values of the absorption coefficient of adipose tissue ($\mu_{adi}(\lambda)$) are shown in Figure 7(b). The absorption coefficient of the subcutaneous fat layer ($\mu_{a_f}(\lambda)$) can be defined as:

$$\mu_{a_f}(\lambda) = V_{adi} \mu_{adi}(\lambda) + (1 - V_{adi}) \mu_w(\lambda) + (1 - V_{adi})(1 - V_w) \mu_b(\lambda) \tag{10}$$

where $\mu_m(\lambda)$ is the absorption coefficient of melanin and $\mu_b(\lambda)$ is the baseline absorption coefficient (the inherent absorption qualities of the skin in the absence of any other chromophores). $\mu_{A_i}(\lambda)$ and $\mu_{V_i}(\lambda)$ represent the arterial and venous blood absorption which varies in different dermis layers, respectively, calculated as:

$$\mu_m(\lambda) = 6.6 \times 10^{10} \times \lambda^{-3.33} \tag{11}$$

$$\mu_b(\lambda) = 7.84 \times 10^7 \times \lambda^{-3.325} \tag{12}$$

$$\mu_A(\lambda) = SaO_2 \mu_{HbO_2}(\lambda) + (1 - SaO_2) \mu_{HHb}(\lambda) \tag{13}$$

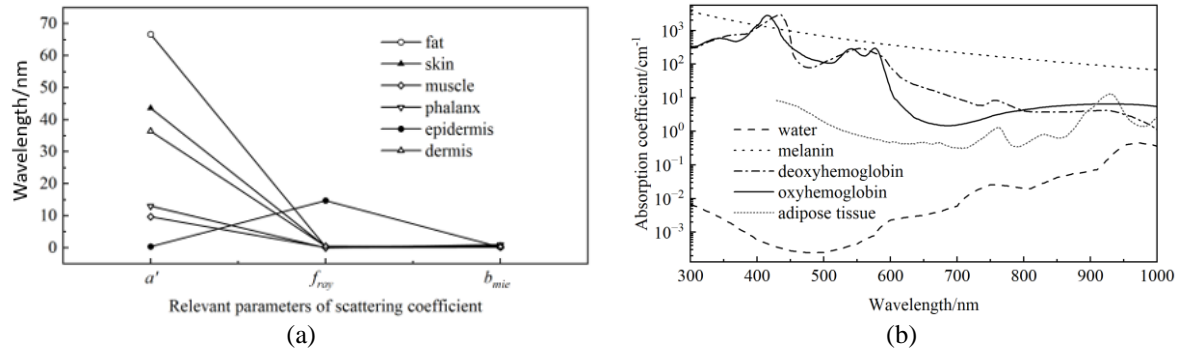$$\mu_V(\lambda) = SvO_2 \mu_{HbO_2}(\lambda) + (1 - SvO_2) \mu_{HHb}(\lambda) \tag{14}$$

Figure 7. Related parameters of (a) absorption coefficient of the four chromophores and adipose tissue and (b) scattering coefficient

Based on Kwon *et al.* [15] on the relationship between skin optical coefficient and uniform compression on the skin, the variables $\mu_a(\lambda)$ and $\mu_{a,p}(\lambda)$, $\mu_s(\lambda)$ and $\mu_{s,p}(\lambda)$ are used to denote the absorption and scattering coefficient before and after deformation, while d_i and $d_{i,p}$ represent the tissue thickness. The interdependence between thickness, absorption coefficient, and scattering coefficient is characterized by (15) and (16).

$$\mu_{a,p}(\lambda) = \mu_a(\lambda)\left(\frac{d_i}{d_{i,p}}\right)^\alpha \tag{15}$$

$$\mu_{s,p}(\lambda) = \mu_s(\lambda)\left(\frac{d_i}{d_{i,p}}\right)^\alpha \tag{16}$$

The study examines the correlation between the experimentally measured photon density and the model simulation results when different values of α are used, and the results indicate that when the value is 0.7, the error between the simulation results and the experimental measurements is the smallest; therefore, the optical modeling parameters were set to be $\alpha = 0.7$ in this paper.

2.5. MC simulation

Compared with the existing methods, such as radiative transfer theory and diffuse approximation, the MC simulates the light propagation in tissues with rigorousness and accuracy that fits better with real data [29]. It is also simpler to deal with the light transmission in a deformed finger under pressure when using the MC model since it offers more freedom in modeling the geometry shape and defining the optical properties of the medium. It has become one of the principal research methods for tissue optical distribution [32]. MC determines the probability distribution model of photon movement (direction and step size) based on the optical properties of the tissues and achieves the simulation of several physical quantities by counting the stochastic motion processes of generous photons, which in this paper are mainly manifested in the reflected and transmitted light intensities. The accuracy of the model can be quantified by its convergence rate, which is defined as $1/\sqrt{C}$, where C is the number of photons in the simulation run [33], and is taken to be $C = 10^8$ in this paper, leading to a convergence rate of 0.0001. The large number of photon iterations makes the results reliable and accurate.

The MC model was implemented in two modalities, modeling spectral acquisition systems for reflectance and transmittance PPG [34] in the index finger at the wavelength of 660 nm and 940 nm, as represented in Figure 6. In the reflectance mode, the light source and detector were positioned on the same side of the measurement location. In the transmittance mode, they were put on two opposite sides of the skin surface [35], simulating a Gaussian beam with a 10mm radius which was perpendicular to the skin. To simulate the 'pulse', the arterial blood volume in diastole was set as half of systole. Executed the model to quantify the reflected and transmitted photons at 660 nm and 940 nm, and recorded the intensity of the detected photon packets. The difference between diastole and systole is known as pulsatile density, that is, 'pulse'. The normalized pulsatile density is calculated by the ratio of 'pulse' and the photon density of diastole.

$$P(\lambda) = \frac{P_{diastole}(\lambda) - P_{systole}(\lambda)}{P_{diastole}(\lambda)} \tag{17}$$

The model code in this paper was created in MATLAB MathWorks (Inc., Natick, MA, USA). It referred to the MC simulation of multi-layer biological tissues with embedded objects (MCML-EO) [36]. According to previous findings upon the deformation of each tissue layer under pressure with its influence on the optical parameters, the MC can be used to simulate the transmission and reflection of light before and after deformation, so as to quantitative analysis of the impact of contact pressure on the collection of reflected and transmitted PPG.

3. RESULTS AND DISCUSSION

3.1. Tissue deformation

During the process of deformation under external pressure, there are two primary changes in the skin: the compression of skin thickness and the increase in optical coefficient. The material of human skin demonstrates significant nonlinearity and anisotropy, the parameters of linear and nonlinear models to characterize the material properties of skin would be influenced by several factors such as age, race, gender, emotions, and environmental circumstances, the values can exhibit significant variations over 4 to 5 orders (4.4 kPa-57 MPa) [16]. Hence, before reproducing fingertip pressing behavior by the model, it is imperative to ascertain the skin material properties of the subject under the current experimental conditions.

After executing the chosen POA algorithm, the optimal parameter for simulating the finger pressing behavior was obtained as (955500, 148000, 49560, 0.40, 0.61). In this parameter combination, the objective function found an optimal value of 2,094 mm^4. When the model's input force is depicted in Figure 8, the model was executed to acquire the deformation of each layer during the pressure application procedure, as shown in Figure 9. It is seen that the dermis deformation is most evident when subjected to external mechanical pressure, followed by subcutaneous tissue. The epidermis is mostly composed of keratinocytes and has a relatively thin thickness, it is not significantly deformed. The Young's modulus of nail and phalanx exhibits a significant magnitude, the deformation can be ignored almost. The evolutionary trend aligns with the finding of Reistad [8], who investigated the impact of probe pressure on the diffuse reflectance spectrum of human skin and observed a similar behavior in tissue deformation.
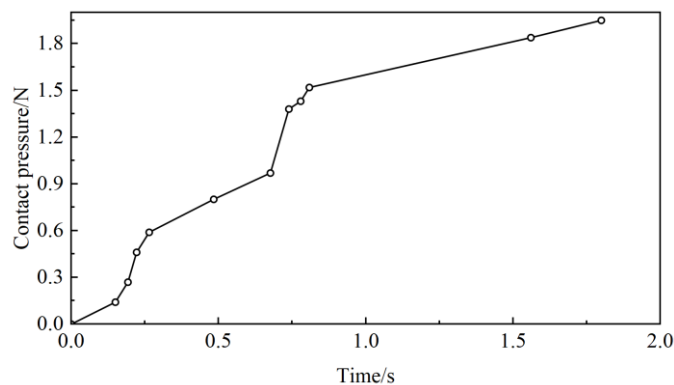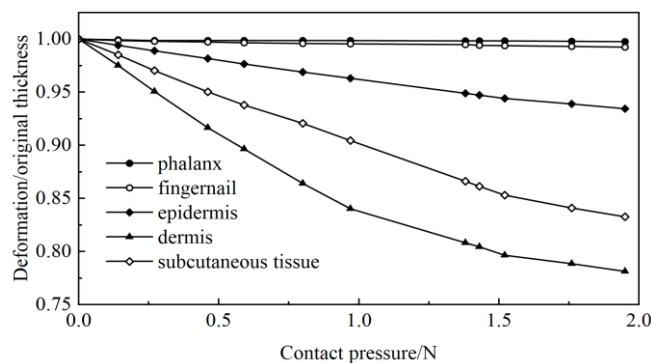

Figure 8. Input force of the FEM model

Figure 9. The thickness changes of each layer

3.2. Optical parameter variations under pressure

When uniformly compressed, the thickness of skin layers decreased along with an increase in its optical coefficients (scattering and absorption). Figures 10 and 11 depict the evolution of the scattering and absorption coefficients of different skin layers as pressure is applied at 660 nm (red light) and 940 nm (infrared light). In MC simulation, the influence of phalanx deformation on its optical parameters is ignored. The simulation results in Figures 10(a) and 11(a) indicate that, as pressure is progressively increased, the scattering coefficients of the skin increase by 18.85% and 13.845%, respectively, at both wavelengths of 660 nm and 940 nm. The variation of the absorption coefficient is shown in Figures 10(b) and 11(b), the changes caused by pressure are mainly in the dermis. Variations in the optical coefficient resulting from skin compression exhibit differences across different wavelengths. An increase of optical coefficient creates challenges to light propagation, and thus impeding the increase in photon density [9]. The reduction in skin thickness competes with the increase in optical coefficient, ultimately influencing the spectral signal detected.
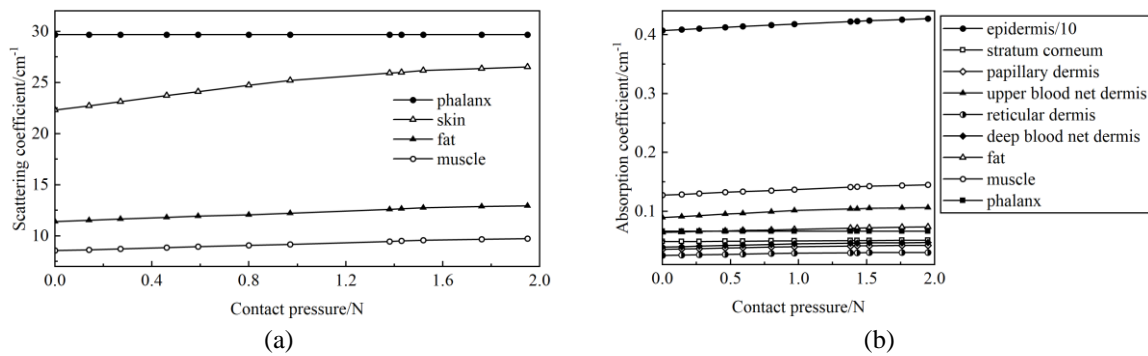

Figure 10. Changes in the optical parameters at 660 nm of (a) scattering coefficient and (b) absorption coefficient
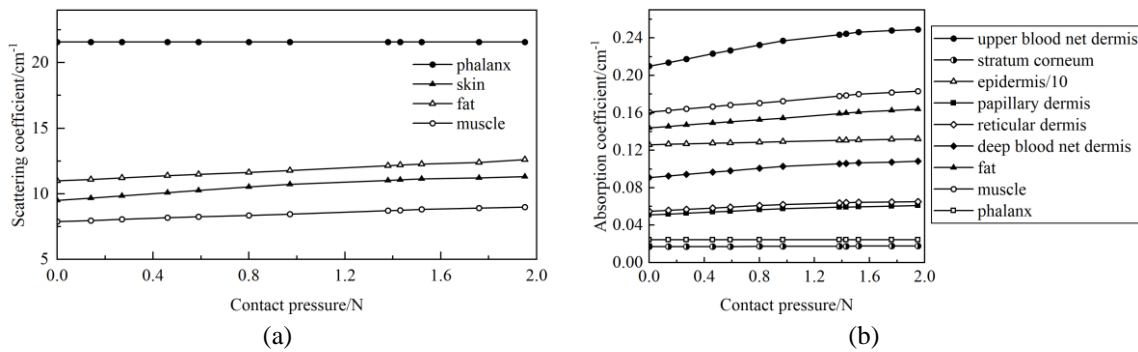

Figure 11. Changes in the optical parameters at 940 nm of (a) scattering coefficient and (b) absorption coefficient

3.3. PPG variations

The reflectance and transmittance of photons at 660 nm and 940 nm were simulated by MC, based on the analytical findings of optical parameters. The results are represented in Figures 12 and 13. The normalized reflectance and transmittance without pressure were compared with the results from the MCML-EO. The difference between the two models is 0.00076 and 0.00091 for the normalized reflectance, 0.00185 and 0.00141 for normalized transmittance, at 660 nm and 940 nm, respectively. The results show the validity of the MC model in this paper. A comparison of the results of Figures 12(a) and 12(b) shows that the transmittance is always higher than the reflectance for systolic and diastolic at red and infrared wavelengths. At both wavelengths, the light intensity during diastole is greater than the systole. After pressure is applied, the reflection at the two wavelengths decreases with the increase of the absorption coefficient both in diastole and systoles, and the change in the red light is more significant compared to the near-infrared light. Figures 13(a) and 13(b) depict the normalized reflectance and transmittance calculated in this paper. At 660 nm,

the normalized reflectance decreased by 1.97%; at 940 nm, there is a 0.49%-5% increase between 0 N and 1.52 N, and the maximum value is reached at 0.46 N. The increase in contact pressure has a positive effect on the normalized transmittance at 660 nm, and this effect gradually stabilizes after 1.52 N. The normalized transmittance at 940 nm increases steadily under pressure and stabilizes at 1.84 N. This indicates that the effect of external pressure on PPG is a wavelength-dependent phenomenon, and that the research results are consistent with those of [37], [38]. Teng and Zhang [37] studied the pulse amplitude of PPG signals gathered from fingertips (880 nm, reflection PPG) while the contact force increased from 0.2 N to 1.8 N, the results showed that various subjects reached maximal PPG amplitudes at various contact pressures (0.2-1.0 N), and Lee *et al.* [38] ascertained this range to be 0.4-0.6 N.

The pulsatile portion of the PPG received by photodetectors in both transmission and reflection modes arises primarily from several vascular factors, represented as changes in blood volume under the analytical model developed in this paper. Shimojo *et al.* [25] used a hierarchical model to measure light distribution in the epidermis, dermis, and subcutaneous tissues. The results showed that photons with wavelengths between 405 and 532 nm reach the upper dermis, while light in 595-800 nm penetrates into the dermis's deeper layers. Photons with wavelengths from 900 nm to longer can reach the subcutaneous fat, where small arteries and arterioles are a richer source of PPG. Shimojo's findings could explain the higher transmittance at 940 nm than at 660 nm, while Chen *et al.* [39] points out that the compression of the skin leads to the photons penetrating deeper and reaching more pulsating blood vessels, and that the intensity of transmitted light keeps increasing with the application of pressure, as shown in Figures 12(b) and 13(b).

Li *et al.* [9], Liu *et al.* [33], and Reuss [40], suggest that only the dermis affects PPG formation, ignoring the role of blood vessels in it in deeper layers. Finlayson *et al.* [24] report on the relationship between light penetration depth and wavelength demonstrated the involvement of the dermis and subcutaneous tissue in PPG formation. A new hypothesis about the origin of PPG has emerged, that is, the reflected PPG signal is a mixture of the blood characteristics of the dermis and subcutaneous tissue. Based on this theory, Moco *et al.* [14] created a six layers MC model of skin, including the subcutaneous fat layer, and analyzed the changes of reflectance spectra before and after the skin was compressed, and found that the reflectance spectra showed a decreasing tendency in the wavelength range of 450-1,000 nm, and the shorter the wavelength, the more obvious it becomes. This is consistent with the findings of this paper, where the reflectance at 660 nm and 940 nm decreased by 15.74% (systolic), 17.89% (diastolic) and 15.18% (systolic), 15.62% (diastolic) before and after the application of contact pressure, respectively. The dermis is the source of the reflected photons at 660 nm wavelength, and blood flow in capillaries, veins, and part of arterioles is mostly responsible for the pulse [41]. The current broad opinion about the origin of PPG states that the arteries and arterioles are primarily responsible for the variations of tissue optical density during the cardiac beat cycle, and the effect of veins and capillaries in the single blood circulation cycle is insignificant by contrast [29]. Additionally, as shown in Figures 10 and 11, the epidermis's absorption is predominant at 660 nm, with little influence from the dermis's layers storing blood information. This allows the pulsatile portion of the reflected light to decrease when pressure is applied. For the 940 nm wavelength, photons are transmitted to the subcutaneous fat layer, which is rich in blood information. Meanwhile, the scattering coefficient of the fat layer is higher than that of the skin, and more photons scattered back to the skin's surface come from the fat layer, bringing about stronger pulsatile information, corresponding to the increase in normalized reflection. Systolic events correspond to the blood reflux in the skin tissue, which is represented in the model as a small increment in the absorption and scattering coefficients of the different tissue layers compared to diastole [42], making the PPG signal smaller in systole than in diastole.

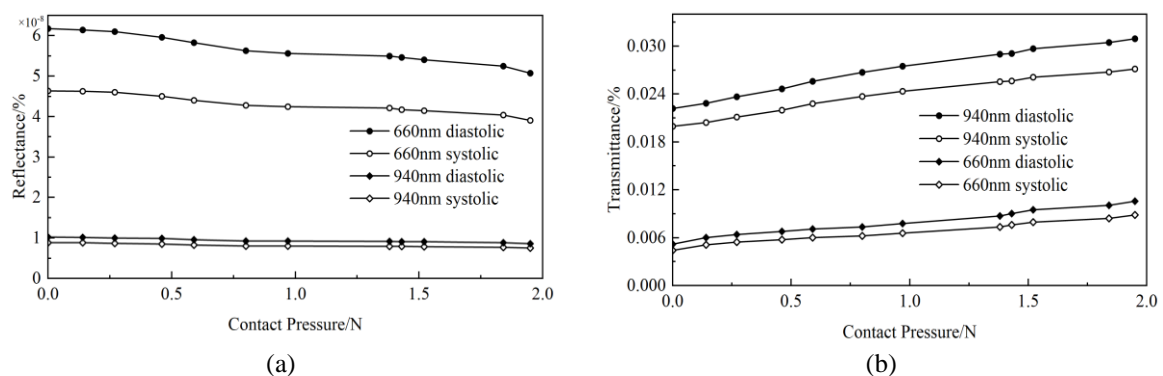(a)   (b)

Figure 12. The optical simulation results of the MC model in (a) reflectance and (b) transmittance
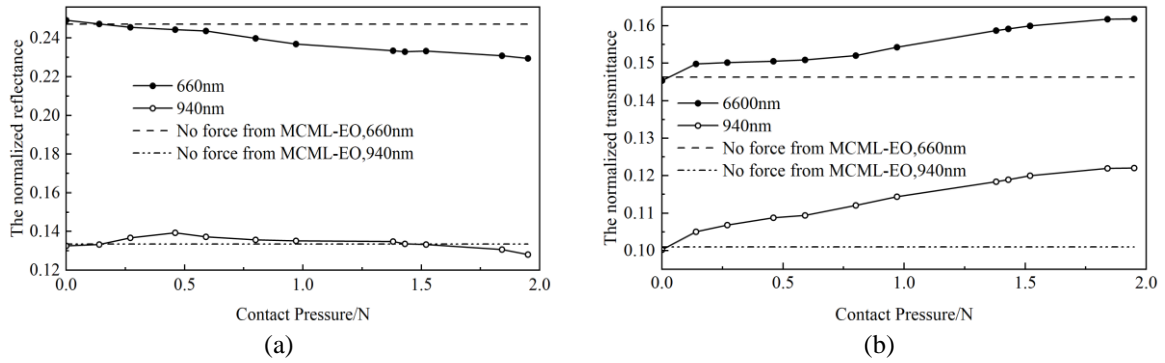
Figure 13. The optical simulation results of the MC model in (a) normalized reflectance and (b) normalized transmittance

3.4. Oxygen saturation analysis

Pulse wave oximetry is commonly employed for the assessment of blood oxygen saturation. The fundamental concept is to develop a correlation between normalized PPG amplitude ratios at red and near-infrared wavelengths and blood oxygen levels. This paper defined the ratio of normalized pulsation intensity at 660 nm and 940 nm as (18):

$$I = \frac{P(660\ nm)}{P(940\ nm)} \tag{18}$$

commercial pulse oximeters are typically calibrated in a blood oxygen saturation range of 70 to 100% [43]. The empirical calibration curve of the commerical pluse oximeter is denoted by the formula about ratio I, expressed as (19):

$$C_{SpO_2} = 110 - 25I \tag{19}$$

C_{SpO_2} represents the blood oxygen saturation. To obtain the transmittance and its normalized value, run an MC simulation of the transmission mode in a working state without pressure application and a blood oxygen saturation of 70-100%. The simulated results of transmittance and the normalized transmittance are illustrated in Figures 14 and 15. The ratio I under the current setting is determined using (18). Following this, A linear fit to the simulated data points of blood oxygen saturation and ratio I, the simulated empirical calibration curve is shown in Figure 16, expressed as (20).

$$C_{SaO_2} = 109.45 - 27.04I \tag{20}$$

The Pearson correlation value between the two curves is 0.9993, indicating a strong positive relationship between the simulated data and the reference empirical calibration curve. Figure 17 shows the ratio I for the scope of experimental pressure at 70% blood oxygen content. The blood oxygen saturation under pressure was calculated using the fitted curve, as presented in Figure 18.
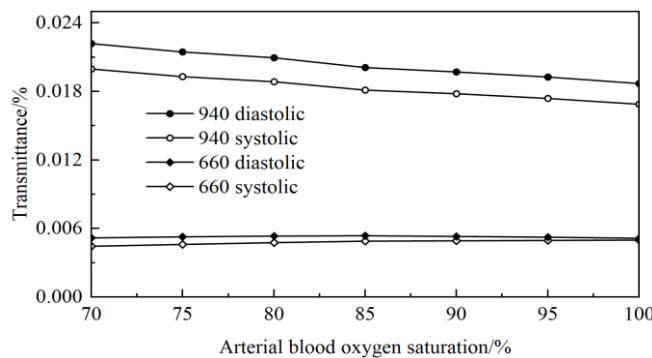

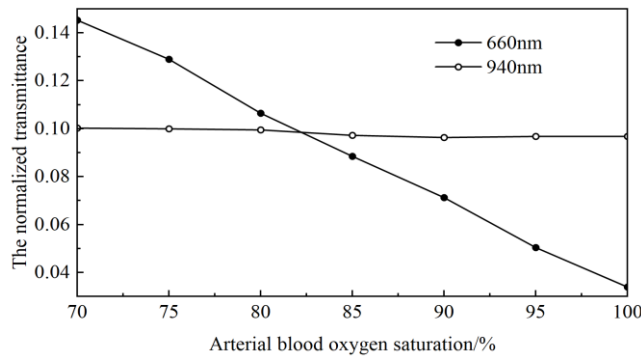Figure 14. Detected transmittance at different blood oxygen levels

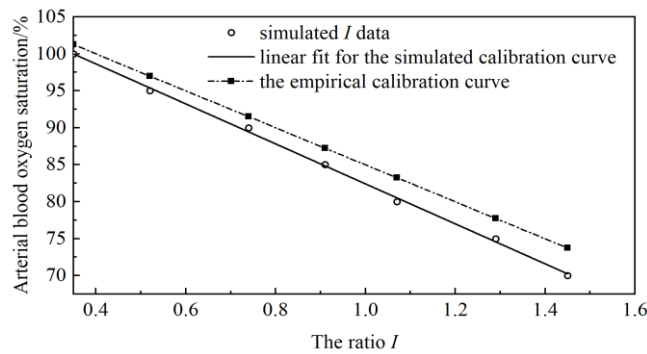Figure 15. The normalized transmittance at different blood oxygen levels

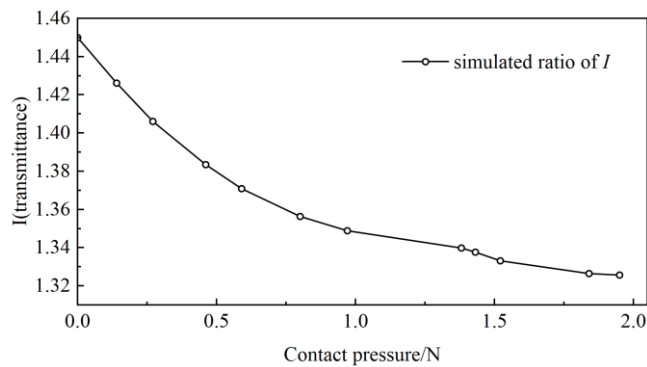Figure 16. Comparison of calibration curves simulated by MC with commercial calibration curves

Figure 17. Variation in the ratio *I* under pressure at 70% blood oxygen saturation

There is a 4.19% to 4.76% deviation between the content of blood oxygen derived from the two curves, and the impact of the pressure can induce a variation of 0.35% to 6.2%. The presented data matches findings from previous research [44] (in small loads, Santos' study demonstrated a 7% variation, utilizing wavelengths of 660 nm and 905 nm; Similarly, Dresher's research yielded a result of 5.1%). When setting up the empirical calibration curve for oximetry, it is imperative to consider the impact of this pressure-induced variation. As the dynamic contact of the finger is a complex process, several factors contribute to the change in the pulse fluctuation $(P_{diastole}(\lambda) - P_{systole}(\lambda))$. These factors primarily include the dynamic changes in the finger's layers caused by the pressure and the changes in the number of effective photons related to the blood composition due to the pressure application-effective photons being defined in this study as the transmissive photons. The increase in photons associated only with changes in blood composition contributes to the detection of blood oxygenation, and the mechanism by which this change in blood oxygen saturation is produced needs to be further analyzed by controlling the variables.
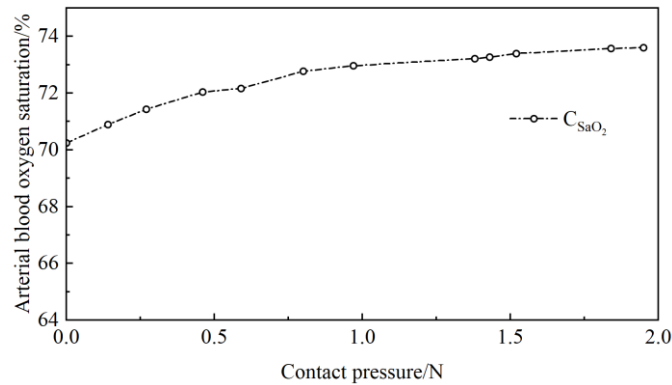
Figure 18. Variations of blood oxygen content under pressure

4. CONCLUSION

Owing to the significance of contact pressure in blood components detection and the limitations of previous research, a finger finite element and MC connection simulation model was developed to analyze the effect of skin thickness changes caused by contact pressure between the fingertip and the light sensor on transmittance and reflectance PPG signals during the process of pulse wave acquisition. The finger FEM in contact with the sensor reproduces the deformation of each tissue layer during finger compression, which is used to calculate the absorption and scattering coefficients of the skin. Then the effects of various pressures on the optical signals during diastole and systole are analyzed, while PPG signals are collected at wavelengths of 660 nm and 940 nm, using MC simulation in the state of 70% blood oxygen saturation and 13% melanin content. The results show that the effect of tissue compression on the optical properties of fingertip skin is wavelength-dependent, the gradual decrease of diffuse reflectance spectroscopy under pressure is accompanied by an increase in transmittance light. The pressure settings that maximize the normalized amplitude of reflected and transmitted light are 0 N (660 nm), 0.46 N (940 nm) and 1.52 N (660 nm), 1.84 N (940 nm), after processing and analyzing the data received from modeling the process of reflected and transmitted light. The blood oxygen saturation research shows that there will be a 0.35-6.2% variation in the sensor's detection when there is pressure of 0-2 N, this variation increases as pressure is applied and trends to stabilize after 1.84 N, which is consistent with the evolutionary trend of the normalized transmitted light at both two wavelengths. Before designing a spectral detection system, this study can be used to analyze the impact of contact pressure on PPG amplitude at selected wavelengths. For different blood components, the impact needs to be studied in more detail by combining different principles of component analysis. The influence of several demographic factors, such as skin color (specifically melanin and blood oxygen concentration) and thickness, on the detected PPG signals varies across different populations. Future studies will be undertaken to explore this matter in greater detail.

REFERENCES

[1] I. Fine and A. Kaminsky, "Scattering-driven PPG signal model," *Biomedical Optics Express,* vol. 13, no. 4, pp. 2286–2298, 2021, doi: 10.1101/2021.06.22.449402.
[2] M. Elgendi, "On the analysis of fingertip photoplethysmogram signals," *Current Cardiology Reviews,* vol. 8, no. 1, pp. 14–25, 2012, doi: 10.2174/157340312801215782.
[3] C. F. Pinto, J. S. Parab, M. D. Sequeira, and G. Naik, "Improving hemoglobin estimation accuracy through standardizing of light-emitting diode power," *International Journal of Electrical and Computer Engineering,* vol. 12, no. 1, pp. 219–228, 2022, doi: 10.11591/ijece.v12i1.pp219-228.
[4] H. Shen, X. Gu, and Y. Wu, "A fingertip-type magnetic pulse detection device for unusual monitoring conditions," *Commun English,* vol. 2, no. 1, pp. 1–9, 2023, doi: 10.1038/s44172-023-00102-2.
[5] B. Haryadi, P.-H. Chang, A. Akrom, A. Q. Raharjo, and G. Prakoso, "Poincaré plots to analyze photoplethysmography signal between non-smokers and smokers," *International Journal of Electrical and Computer Engineering (IJECE),* vol. 12, no. 2, pp. 1565–1570, 2022, doi: 10.11591/ijece.v12i2.pp1565-1570.
[6] D. Ray, T. Collins, S. Woolley, and P. Ponnapalli, "A review of wearable multi-wavelength photoplethysmography," *IEEE Reviews in Biomedical Engineering,* vol. 16, pp. 136–151, 2023, doi: 10.1109/rbme.2021.3121476.

[7] R. A. Firmansyah, Y. A. Prabowo, T. Suheta, and S. Muharom, "Implementation of 1D convolutional neural network for improvement remote photoplethysmography measurement," *Indonesian Journal of Electrical Engineering and Computer Science (IJEECS),* vol. 29, no. 3, pp. 1326–1335, 2023, doi: 10.11591/ijeecs.v29.i3.pp1326-1335.

[8] C. Kurachi *et al.*, "Characterization of probe contact effects on diffuse reflectance spectroscopy measurements," in Biophotonics South America, 2015, pp. 953143, doi: 10.1117/12.2180917.

[9] C. X. Li, J. Y. Jiang, R. Liu, W. L. Chen, and K. X. Xu, "Research on the influence of pressure-induced skin deformation on the diffuse re-flection spectra measurement," *Spectroscopy and Spectral Analysis,* vol. 37, no. 10, pp. 3006–3010, 2017, doi: 10.3964/j.issn.1000-0593(2017)10-3006-05.

[10] A. A. Kamshilin *et al.*, "A new look at the essence of the imaging photoplethysmography," *Scientific Reports,* vol. 5, no. 1, pp. 1–9, 2015, doi: 10.1038/srep10494.

[11] J. M. May, E. Mejía-Mejía, M. Nomoni, K. Budidha, C. Choi, and P. A. Kyriacou, "Effects of contact pressure in reflectance photoplethysmography in an in vitro tissue-vessel phantom," *Sensors,* vol. 21, no. 24, pp. 8421, 2021, doi: 10.3390/s21248421.

[12] L. Lim, B. Nichols, N. Rajaram, and J. W. Tunnell, "Probe pressure effects on human skin diffuse reflectance and fluorescence spectroscopy measurements," *Journal of Biomedical Optics,* vol. 16, no. 1, pp. 011012, 2011, doi: 10.1117/1.3525288.

[13] R. Reif, M. S. Amorosino, K. W. Calabro, O. A'Amar, S. K. Singh, and I. J. Bigio, "Analysis of changes in reflectance measurements on biological tissues subjected to different probe pressures," *Journal of Biomedical Optics,* vol. 13, no. 1, pp. 010502, 2008, doi: 10.1117/1.2870115.

[14] A. V. Moço, S. Stuijk, and G. de Haan, "New insights into the origin of remote PPG signals in visible light and infrared," *Scientific Reports,* vol. 8, no. 1, pp. 8501, 2018, doi: 10.1038/s41598-018-26068-2.

[15] K. Kwon, T. Son, K.-J. Lee, and B. Jung, "Enhancement of light propagation depth in skin: cross-validation of mathematical modeling methods," *Lasers in Medical Science,* vol. 24, no. 4, pp. 605–615, 2008, doi: 10.1007/s10103-008-0625-4.

[16] S. Nam and K. J. Kuchenbecker, "Optimizing a viscoelastic finite element model to represent the dry, natural, and moist human finger pressing on glass," (in English), *IEEE Transactions on Haptics,* vol. 14, no. 2, pp. 303–309, 2021, doi: 10.1109/Toh.2021.3077549.

[17] F. Shao, T. H. C. Childs, C. J. Barnes, and B. Henson, "Finite element simulations of static and sliding contact between a human fingertip and textured surfaces," *Tribology International,* vol. 43, no. 12, pp. 2308–2316, 2010, doi: 10.1016/j.triboint.2010.08.003.

[18] M. L. D'Angelo *et al.*, "An integrated approach to characterize the behavior of a human fingertip in contact with a silica window," *IEEE Transactions on Haptics,* vol. 10, no. 1, pp. 123–129, 2017, doi: 10.1109/toh.2016.2614679.

[19] T. Hamasaki and M. Iwamoto, "Computational analysis of the relationship between mechanical state and mechanoreceptor responses during scanning of a textured surface," *Advances in Mechanical Engineering,* vol. 11, no. 11, pp. 1–13, 2019, doi: 10.1177/1687814019885263.

[20] S. J. Mostafavi Yazdi and J. Baqersad, "Mechanical modeling and characterization of human skin: A review," *Journal of Biomechanics,* vol. 130, pp. 110864, 2022, doi: 10.1016/j.jbiomech.2021.110864.

[21] S. Nam, Y. Vardar, D. Gueorguiev, and K. J. Kuchenbecker, "Physical variables underlying tactile stickiness during fingerpad detachment," *Frontiers in Neuroscience,* vol. 14, no. 2, pp. 303–309, 2020, doi: 10.3389/fnins.2020.00235.

[22] S. Kumar, G. Liu, D. W. Schloerb, and M. A. Srinivasan, "Viscoelastic characterization of the primate finger pad in vivo by microstep indentation and three-dimensional finite element models for tactile sensation studies," *Journal of Biomechanical Engineering,* vol. 137, no. 6, pp. 061002, 2015, doi: 10.1115/1.4029985.

[23] L. Zhou, S. B. Wang, L. A. Li, Z. Y. Wang, and C. W. Li, "Advances in skin mechanics," *Experimental Mechanics,* vol. 35, no. 06, pp. 955–969, 2020, doi: 10.7520/1001-4888-19-165.

[24] L. Finlayson *et al.*, "Depth penetration of light into skin as a function of wavelength from 200 to 1000 nm," *Photochemistry and Photobiology,* vol. 98, no. 4, pp. 974–981, 2021, doi: 10.1111/php.13550.

[25] Y. Shimojo, T. Nishimura, H. Hazama, T. Ozawa, and K. Awazu, "Measurement of absorption and reduced scattering coefficients in Asian human epidermis, dermis, and subcutaneous fat tissues in the 400- to 1100-nm wavelength range for optical penetration depth and energy deposition analysis," *Journal of Biomedical Optics,* vol. 25, no. 04, pp. 045002, 2020, doi: 10.1117/1.Jbo.25.4.045002.

[26] S. Chatterjee, K. Budidha, and P. A. Kyriacou, "Investigating the origin of photoplethysmography using a multiwavelength Monte Carlo model," *Physiological Measurement,* vol. 41, no. 8, pp. 084001, 2020, doi: 10.1088/1361-6579/aba008.

[27] C. Ash, M. Dubec, K. Donne, and T. Bashford, "Effect of wavelength and beam width on penetration in light-tissue interaction using computational methods," *Lasers in Medical Science,* vol. 32, no. 8, pp. 1909–1918, 2017, doi: 10.1007/s10103-017-2317-4.

[28] S. Chatterjee and P. Kyriacou, "Monte carlo analysis of optical interactions in reflectance and transmittance finger photoplethysmography," *Sensors,* vol. 19, no. 4, pp. 789, 2019, doi: 10.3390/s19040789.

[29] Y. Jing *et al.*, "Simulation analysis of skin diffuse reflectance spectroscopy and skin color with blood component change," *Acta Optica Sinica,* vol. 42, no. 8, pp. 0817001, 2022, doi: 10.3788/aos202242.0817001.

[30] S. L. Jacques, "Corrigendum: optical properties of biological tissues: a review," *Physics in Medicine and Biology,* vol. 58, no. 14, pp. 5007–5008, 2013, doi:10.1088/0031-9155/58/14/5007.

[31] K. Setchfield, A. Gorman, A. H. R. W. Simpson, M. G. Somekh, and A. J. Wright, "Relevance and utility of the in-vivo and ex-vivo optical properties of the skin reported in the literature: a review," *Biomedical Optics Express,* vol. 14, no. 7, pp. 3555–3583, 2023, doi: 10.1364/boe.493588.

[32] V. Periyasamy and M. Pramanik, "Monte Carlo simulation of light transport in tissue for optimizing light delivery in photoacoustic imaging of the sentinel lymph node," *Journal of Biomedical Optics,* vol. 18, no. 10, pp. 106008, 2013, doi: 10.1117/1.Jbo.18.10.106008.

[33] W. B. Liu, J. Liu, T. S. Han, Q. Ge, and R. Liu, "Simulation of the effect of dermal thickness on non-invasive blood glucose measurement by near-infrared spectroscopy," *Spectroscopy and Spectral Analysis,* vol. 43, no. 9, pp. 2699–2704, 2023, doi: 10.3964/j.issn.1000-0593(2023)09-2966-06.

[34] S. L. Jacques, "Tutorial on monte carlo simulation of photon transport in biological tissues [Invited]," *Biomedical Optics Express,* vol. 14, no. 2, pp. 559–576, 2023, doi: 10.1364/boe.477237.

[35] T. Y. Abay and P. A. Kyriacou, "Reflectance photoplethysmography as noninvasive monitoring of tissue blood perfusion," *IEEE IEEE Transactions on Biomedical Engineering,* vol. 62, no. 9, pp. 2187–2195, Sep 2015, doi: 10.1109/Tbme.2015.2417863.

[36] V. Periyasamy and M. Pramanik, "Monte Carlo simulation of light transport in turbid medium with embedded object—spherical, cylindrical, ellipsoidal, or cuboidal objects embedded within multilayered tissues," *Journal of Biomedical Optics,* vol. 19, no. 4, pp. 045003, 2014, doi: 10.1117/1.Jbo.19.4.045003.

[37] X. F. Teng and Y. T. Zhang, "The effect of contacting force on photoplethysmographic signals," *Physiological Measurement,* vol. 25, no. 5, pp. 1323–1335, 2004, doi: 10.1088/0967-3334/25/5/020.

[38] J. H. Lee *et al.*, "Time to consider the contact force during photoplethysmography measurement during pediatric anesthesia: A prospective, nonrandomized interventional study," *Pediatric Anesthesia,* vol. 28, no. 7, pp. 660–667, 2018, doi: 10.1111/pan.13415.

[39] Y. Y. Chen, S. Y. Tzeng, Y. Y. Yen, N. Y. Cheng, and S.-H. Tseng, "Non-invasive assessment of skin hydration and sensation with diffuse reflectance spectroscopy," *Scientific Reports,* vol. 13, no. 1, pp. 20149, 2023, doi:10.1038/s41598-023-47349-5.

[40] J. L. Reuss, "Multilayer modeling of reflectance pulse oximetry," *IEEE Transactions on Biomedical Engineering,* vol. 52, no. 2, pp. 153–159, 2005, doi: 10.1109/tbme.2004.840188.

[41] Y. Rong, P. C. Theofanopoulos, G. C. Trichopoulos, and D. W. Bliss, "A new principle of pulse detection based on terahertz wave plethysmography," *Scientific Reports,* vol. 12, no. 1, pp. 6347, 2022, doi: 10.1038/s41598-022-09801-w.

[42] M. A. Al-Dhaheri, N. E. Mekkakia-Maaza, H. Mouhadjer, and A. Lakhdari, "Noninvasive blood glucose monitoring system based on near-infrared method," *International Journal of Electrical and Computer Engineering,* vol. 10, no. 2, pp. 1736–1746, 2020, doi: 10.11591/ijece.v10i2.pp1736-1746.

[43] R. Al-Halawani, P. H. Charlton, M. Qassem, and P. A. Kyriacou, "A review of the effect of skin pigmentation on pulse oximeter accuracy," *Physiological Measurement,* vol. 44, no. 5, pp. 05TR01, 2023, doi:10.1088/1361-6579/acd51a.

[44] V. A. P. Santos, J. Cardoso, and C. Correia, "Photoplethysmographic logger with contact force and hydrostatic pressure monitoring," in *2013 IEEE 3rd Portuguese Meeting in Bioengineering,* 2013, pp. 1–6, doi: 10.1109/ENBENG.2013.6518437.

BIOGRAPHIES OF AUTHORS

Xin Gong 🆔 🇬 SC ᑕ is a graduate student at the School of Electrical and Electronic Engineering at Chongqing University of Technology, specializing in blood composition analysis and processing. Her research field is blood information acquisition and image/information processing, and she has won the second prize in the 2022 Asia Pacific Mathematical in Modeling and the "Huashu cup" International Mathematical Contest in Modeling. She can be contacted at email: gongxin33036@hotmail.com.

Chengbo Yu 🆔 🇬 SC ᑕ is professor at the School of Electrical and Electronic Engineering, Chongqing University of Technology. He holds a doctoral degree in engineering and specializes in the acquisition and processing of medical information. He is the academic and technical leader of Chongqing, the director of the Remote Testing and Control Technology Research Institute, a member of the National Industrial Process Measurement and Control Standardization Technical Committee, and the Process Testing and Control Instrumentation Branch of the China Instrumentation Society Director of the Microcomputer Application Branch of the China Instrumentation Society, senior members of the China Instrumentation Society, Mechanical Engineering Society, Military Engineering Society, and China Automotive Engineering Society. Published over 150 academic papers (59 papers indexed by SCI, EI, and ISTP), obtained 23 patents (including 8 invention patents), and published over 20 monographs and textbooks. He can be contacted at email: yuchengbo@cqut.edu.cn.

Yiguo Xuan 🆔 🇬 SC ᑕ is a graduate student at the School of Electrical and Electronic Engineering at Chongqing University of Technology, specializing in blood composition analysis and processing. His research field is blood information acquisition and image processing. He can be contacted at email: xuanxuan123456@stu.cqut.edu.cn.